Research Paper

Dynamic simulation and experimental validation of a high-temperature Brayton heat pump

A. Phong Tran [ORCID] *, Panagiotis Stathopoulos

German Aerospace Center (DLR), Institute of Low-Carbon Industrial Processes, Walther-Pauer-Straße 5, Cottbus, 03046, Germany

ABSTRACT

The decarbonization of industrial process heating will require widespread adoption of high-temperature heat pumps. Brayton cycle heat pumps are capable of providing heat at temperatures that currently cannot be achieved by conventional vapor-compression cycle heat pumps. However, significant challenges remain in adapting these systems to industrial applications, particularly with regard to operational safety, control strategies, and flexibility in response to varying operational conditions. This study presents a dynamic model of a closed-loop Brayton cycle heat pump capable of producing temperatures of 250 °C and higher, validated using experimental data. The physics-based model implemented in Modelica captures key thermodynamic processes and system dynamics, including thermal inertia and volume dynamics. An optimization-based method is used to calibrate model parameters, minimizing the error between measured and simulated data. Given the significant impact of the compressor on overall heat pump performance, a novel calibration method is introduced to adjust an existing compressor map using limited measurement data. This approach ensures that the compressor behavior is represented with sufficient accuracy, smoothness, and numerical robustness. The calibrated model achieves mean-normalized root mean squared errors (NRMSE) ranging from 0.12 % to 1.46 % for temperatures, pressures, and mass flow rates. The model is applied to examine the system's start-up and deceleration sequences, offering insights into compressor stability and heat exchanger temperature profiles. These results demonstrate the model's utility for control design, performance evaluation, and stability analysis.

1. Introduction

Greenhouse gas (GHG) emissions have driven global warming, raising global surface temperatures by 1.1 °C compared to pre-industrial levels, with the energy sector and industry being responsible for the majority (58 %) of GHG emissions worldwide [1]. In the EU-28 countries, a significant portion (51 %) of final energy demand is used for heating and cooling, of which 26 % are attributed to space heating and 15 % to industrial process heat. Fossil fuels remain the primary energy source for heating, particularly for high-temperature industrial processes [2]. Heat pumps are widely recognized as a key technology for achieving net-zero GHG emission goals, as their ability to replace fossil fuel-based heating with electrified heating makes them critical to this effort [3].

1.1. High-temperature heat pumps

Heat pumps are typically classified based on temperature level, thermodynamic cycle, and compression method.

In recent years, remarkable progress has been made in extending the temperature range of heat pumps: While Arpagaus et al. [4] reported maximum supply temperatures of 90 °C to 165 °C in their heat

pump data compilation published in 2018, the IEA HPT Annex 58 [5] presented data on heat pump applications with temperatures ranging from 115 °C to 280 °C in 2023. The investigated heat pumps range in Technology Readiness Level (TRL) from 4 to 9, with specific investment costs of 200 to 1200 €/kW. This suggests that high-temperature heat pump technology is well-proven and nearing commercialization.

Most heat pumps are based on the vapor compression cycle, using screw, reciprocating, and turbo compressors, as noted by Arpagaus et al. [4] and Annex 58 [5]. Vapor-compression heat pumps are particularly effective for supplying latent heat demand (e.g. steam generation). This is supported by a study conducted by Ma et al. [6], who reviewed recent advancements and technologies of steam-generating heat pumps. For providing sensible heating with very high supply temperatures, gas compression heat pumps based on the Brayton or Stirling cycles become viable options. The reverse Brayton cycle has several advantages: unlike vapor compression, it does not involve phase changes, so process temperatures are mainly constrained by material limitations and compressor pressure ratio. This flexibility in design and operation, combined with the use of dried air as a working medium (safe, cheap,

---

Nomenclature

a	β function coefficient
A_v	Valve flow coefficient
b	β function coefficient
C	Map correction matrix
c	Map correction matrix coefficient
D	Map correction matrix
d	Map correction matrix coefficient
d_i	Inner tube diameter
F	Turbomachinery map matrix
f	Differential equation function
f	Turbomachinery map function
$\hat{f}$	Differential equation function, ODE form
g	Algebraic equation function
h	Specific enthalpy
k	Scaling factor
L	Characteristic length
$\dot{m}$	Mass flow rate
m	Mass
N	Shaft speed
n_β	Number of β-lines
n_N	Number of speedlines
Nu	Nusselt number
p	Total pressure
Pr	Prandtl number
Re	Reynolds number
T	Temperature
t	Time
V	Volume
x	State variable
$\dot{x}$	State variable derivative
$\bar{y}$	Mean value of signal
$\hat{y}$	Simulated signal
y	Algebraic variable
y	Measured signal

Greek symbols

α	Heat transfer coefficient
β	Compressor map auxiliary coordinate
η	Isentropic efficiency
η_m	Mechanical efficiency
λ	Thermal conductivity
Φ	Valve characteristic
Π	Pressure ratio
ρ	Density
τ	Torque
Θ	Valve opening

Subscripts

3W	Three-way valve
Amb	Ambient
B	Bypass valve
C1	Compressor 1
C2	Compressor 2
c	Corrected (flow, speed)
η	Efficiency
f	Flow
G	Generator

h	Heat transfer
HP	High-pressure
in	Inflowing
init	Initial
is	Isentropic
lin	Linear
M	Motor
out	Outflowing
p	Pressure
quad	Quadratic
std	Reference conditions
T	Turbine

Abbreviations

DAE	Differential–algebraic system of equations
GHG	Greenhouse gas
HTHX	High-temperature heat exchanger
LTHX	Low-temperature heat exchanger
NRMSE	Normalized root mean square error
ODE	Ordinary differential equation
OP	Operating point
PI	Proportional–integral
PTES	Pumped thermal electricity storage
RL	Reinforcement learning
RMSE	Root mean square error
SL	Surge line
SLSQP	Sequential Least Squares Programming
SM	Surge margin
SP	Set-point
TRL	Technology Readiness Level

and low global warming potential), makes Brayton cycle heat pumps attractive. White [7] conducted thermodynamic assessments of Brayton heat pump cycles, concluding that worthwhile performance can be obtained if high turbomachinery efficiencies and low pressure losses are achieved. Economic feasibility has shown to be a major challenge for adoption of heat pumps: Zühlsdorf et al. [8] concluded that Brayton heat pumps are technically feasible for supply temperatures of up to 300 to 400 °C and presented economically feasible scenarios for temperatures of 280 °C. Schlosser et al. [9] reviewed 155 heat pump case studies to identify factors influencing their implementation in industrial processes, focusing on suitable applications, performance models, and economic considerations that may address barriers to wider adoption.

1.2. Dynamic thermo-fluid simulation

Dynamic simulation has become an essential tool for the development, analysis, and optimization of heat pump systems. Various commercial and open-source simulation platforms, including AMESim, Matlab/Simulink, Modelica, and TRNSYS, are commonly used for this purpose. The importance of dynamic heat pump simulation has been highlighted in recent research. For example, Du et al. [10] use a dynamic model of an R290 (propane) heat pump to examine its start-up behavior, while Jiang et al. [11] develop and validate a dynamic model of a two-stage compression heat pump to improve control strategies. Among the available platforms, Modelica has proven to be a suitable framework for thermo-fluid simulations, owing to its flexibility and support for dynamic system modeling. Heat pump simulations benefit from the development of libraries for thermo-fluid simulation. Notable examples for thermo-fluid libraries are the Buildings library [12],

the ThermoPower library [13], TIL Suite [14] and the Modelon Libraries [15]. Several studies have demonstrated the effectiveness of Modelica in heat pump modeling: for example, Poulsen et al. [16] and Meesenburg et al. [17] optimized the operation of cascade heat pump systems, while Wolscht et al. [18] explored the use of transcritical CO_2 heat pumps for power grid load balancing. Furthermore, Modelica-based heat pump models are increasingly integrated into optimal control frameworks, as shown by Aguilera et al. [19]. Brayton-cycle heat pumps have also been studied in the context of pumped thermal electricity storage (PTES). Notably, Yang et al. [20,21] and Frate et al. [22] have developed thermodynamic models and evaluated control strategies for Brayton-based PTES systems.

Dynamic simulation benefits from novelties in modeling and calibration methods. Zhao et al. [23] propose a numerically efficient and accurate heat exchanger model based on frequency domain analysis that can be integrated into dynamic simulation models. Wang et al. [24] present a method for calibrating compressor maps using adaptation factor surfaces, allowing transformations of map data based on both shaft speed and the β value.

The present work builds on the studies by Oehler et al. [25], which investigated the start-up procedure of a Brayton-cycle heat pump (described in Section 2) using a dynamic model, and Pettinari et al. [26], who designed and analyzed a control system capable of controlling the same heat pump under varying boundary conditions.

1.3. Our contributions

High-temperature Brayton-cycle heat pumps are a key technology for industrial processes requiring temperatures of 250 °C and above. However, their development is challenged by the need for accurate dynamic modeling, effective calibration methods, and a deeper understanding of system performance during transient operation. This paper addresses these challenges by tackling the following research questions:

- How can a dynamic model of a high-temperature Brayton-cycle heat pump be developed and validated to accurately represent transient thermodynamic behaviors and system dynamics?
- What methods can be employed to calibrate compressor performance maps effectively, particularly when measurement data are limited, to ensure accurate and robust model predictions?
- How do transient operating conditions, such as start-up and deceleration, impact system performance, including compressor stability and thermal stresses within heat exchangers?

For this purpose, this paper presents a dynamic model of a Brayton-cycle high-temperature heat pump that can produce temperatures of 250 °C and higher, surpassing the limits of conventional heat pump technologies. The first-principles model accounts for key thermodynamic processes and system dynamics such as thermal inertia and volume dynamics. By relying on a physics-based modeling approach, the model enables reliable extrapolation beyond the experimentally validated operating range. A significant contribution of this work lies in the development of novel model calibration methods for dynamic heat pump models. Compressor performance maps are calibrated using a novel optimization-based approach that integrates limited measurement data with manufacturer-provided maps, ensuring accuracy, robustness, and smooth transitions. This method enhances the accuracy and robustness of the overall Brayton-cycle heat pump model, representing a notable advancement in calibration precision over previous works. Model parameters are calibrated by minimizing the errors between simulated and measured signals for temperature, pressure, and mass flow rates using numerical optimization techniques. The validated model is applied to study transient operations, including start-up and deceleration, providing insights into compressor stability and thermal stresses within the heat exchanger. These findings advance the understanding of system dynamics and support the operation and control of high-temperature Brayton-cycle heat pumps.

2. System and test rig description

This work studies a closed-loop Brayton-cycle heat pump using air as working fluid. Fig. 1 is a photo of the heat pump in the test facility in Cottbus, Germany. The following subsections outline the heat pump layout and its components.

2.1. Layout

A schematic diagram of the heat pump is provided in Fig. 2. The system comprises the following key components:

- **Compression System (A)**: The two-stage compression system consists of two radial compressors arranged in series. These are driven by an electric motor via belt drives.
- **High-Temperature Heat Exchanger (B)**: Heat is extracted from the fluid downstream of the compressors in this heat exchanger.
- **Three-Way Valve (C)**: This valve controls the flow through the recuperator (G), which uses the temperature difference between states 2 and 5 to preheat the fluid at state 0.
- **Turbine (D)**: The turbine expands the fluid, recovering power through a generator and cooling the fluid further.
- **Turbine Bypass Valve (E)**: This valve adjusts the resistance within the loop, allowing control over the operating points of the compressors.
- **Low-Temperature Heat Exchanger (F)**: This heat exchanger enables the fluid to absorb residual heat from a heat source or provide process cooling.
- **Recuperator (G)**: After flowing through the low-temperature heat exchanger, the fluid passes through the recuperator, where its temperature is raised before returning to the compressor inlet.

All heat exchangers of the heat pump are shell-and-tube heat exchangers, with the working fluid routed through the tube side to minimize pressure losses within the primary loop. In the recuperator, the low-pressure flow moves through the tube side. The shell-side flow generally follows a counterflow configuration, but the baffles direct it in a crossflow pattern across the tube bundles. For industrial applications, the shell sides of the low- and high-temperature heat exchangers are connected to the heat source and heat sink, respectively. In the test facility, however, the heat source is emulated by a loop system where dried air is continuously circulated and reheated to a specified temperature. Ambient air serves as the heat sink. To examine the effects of varying compressor inlet temperatures, an electric heater is installed upstream of the compressors. However, since the heater was not employed in the present study, it has been excluded from the flow schematic for clarity.

The fluid inventory (total mass of working fluid) in the heat pump can be regulated through the use of a pair of inlet and relief valves. The inlet valve connects a high-pressure buffer tank to the low-pressure section of the heat pump, enabling an increase in the fluid inventory. In contrast, the relief valve, positioned in the high-pressure section, allows for the release of air to the ambient, thereby reducing the fluid inventory. This system enables adjustment of the heat pump's thermal output, while keeping the aerodynamic operating conditions of the turbomachinery unchanged.

2.2. Test rigs

The heat pump was commissioned gradually, with components added and tested one-by-one in the loop to ensure proper functionality and collect performance data. Five configurations were tested, as outlined below:

- **Single compressor test rig**: Compressor 1 connected to a throttle valve.

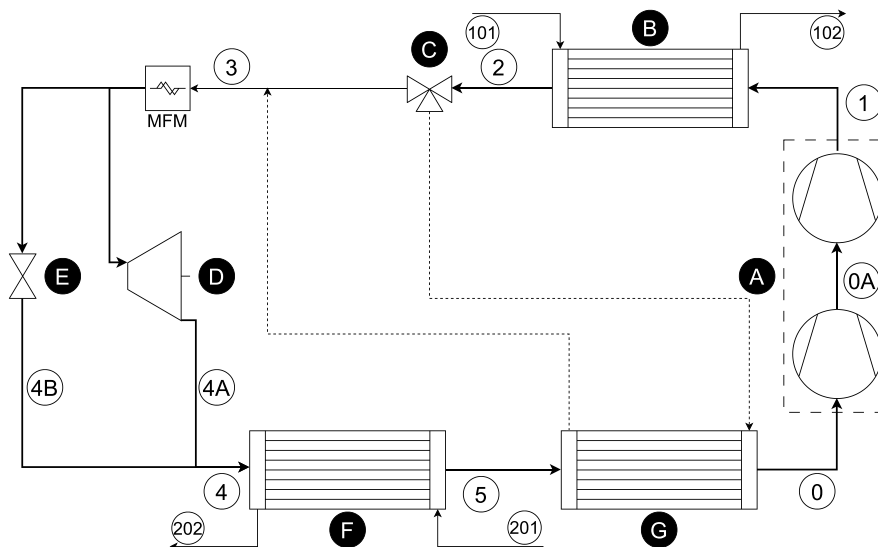**Fig. 1.** Photo of the CoBra heat pump test facility.

Fig. 2. Flow schematic of the CoBra heat pump. (A) Two-stage compression system, (B) high-temperature heat exchanger, (C) three-way valve, (D) turbine, (E) turbine bypass valve, (F) low-temperature heat exchanger, (G) recuperator, MFM: Coriolis mass flow meter.

- **Dual compressor test rig**: Compressor 1 connected to Compressor 2 and a throttle valve.
- **Compressor with HX**: Compressor 1 and Compressor 2 followed by a heat exchanger and a throttle valve.
- **Open-loop heat pump**: Compressor 1 and Compressor 2 connected to a heat exchanger, followed by a turbine and a bypass valve in parallel, venting air to ambient.
- **Closed-loop heat pump**: Closed cycle heat pump as shown in Fig. 2.

This stepwise commissioning allowed the evaluation of individual components and provided data for system modeling and validation.

3. Dynamic modeling

The heat pump model, implemented in Modelica using the Dymola development environment, captures the main system dynamics, such as thermal inertia and volume dynamics. Existing models from the ThermoPower library [13] and the Buildings library [12] are reused, adapted, and extended to fit the requirements of the system. As a

first-principles model, each component model incorporates mass and energy balances to ensure physical consistency. The model is initialized with a preliminary set of parameters, which are subsequently calibrated against test data (see Section 4).

3.1. Turbomachinery

The turbomachinery models are based on the map-based compressor and turbine models from the ThermoPower library [13]. Due to their relatively small size compared to other system components, turbomachinery is represented as steady-state models without inherent volume or thermal dynamics. The equations for mass balance Eq. (1) and enthalpy change Eq. (2) are formulated as follows:

$$\dot{m}_{in} + \dot{m}_{out} = 0 \tag{1}$$

$$h_{out} - h_{in} = \Delta h \tag{2}$$

Here, $\dot{m}_{in}$ and $\dot{m}_{out}$ represent the mass flow rates at the inlet and outlet, h_{in} and h_{out} denote the specific enthalpies of the in- and outflowing streams, and Δh the enthalpy change induced by the turbocomponent. The enthalpy change Δh is determined using the isentropic efficiency η

defined in Eq. (3), where $h_{\text{out,is}}$ denotes the specific outlet enthalpy for an isentropic compression or expansion:

$$\Delta h = \begin{cases} \frac{1}{\eta} \cdot \left(h_{\text{out,is}} - h_{\text{in}} \right) & \text{for compressors} \\ \eta \cdot \left(h_{\text{out,is}} - h_{\text{in}} \right) & \text{for turbines} \end{cases} \tag{3}$$

The change of fluid enthalpy is balanced by the torque applied by or to the rotational mechanical system, as expressed in the energy balance in Eq. (4) with η_{m} denoting the mechanical efficiency, τ the torque and N the mechanical shaft speed:

$$\dot{m}_{\text{in}} \cdot \Delta h = \eta_{\text{m}} \cdot \tau \cdot N \tag{4}$$

The turbomachinery models feature a connection port to rotational mechanical models from the Modelica Mechanics package. This enables the modeling of the motor and generator systems, allowing for simulation of their rotational dynamics, including rotor inertia, gear ratios, and slip, among others.

Flow and rotational speeds are expressed as corrected mass flow rate $\dot{m}_c$ Eq. (5) and corrected speed N_c Eq. (6), based on Mach number similarity principles:

$$\dot{m}_c = \dot{m}\sqrt{T_{\text{in}}}/p_{\text{in}} \tag{5}$$

$$N_c = N/\sqrt{T_{\text{in}}} \tag{6}$$

As initial maps, the compressor models use performance data measured by the manufacturer [27], while the initial turbine maps were obtained from 3D-CFD simulations of the turbine.

3.1.1. Compressor

The compressor performance map consists of three tables, each acting as a lookup table with two independent variables: the corrected speed N_c and the auxiliary coordinate β:

- Corrected mass flow rate $\dot{m}_c$:

$$\dot{m}_c = k_f \cdot f_{\dot{m}_c} \left(N_c, \beta \right) \tag{7}$$

- Pressure ratio $\Pi = p_{\text{out}}/p_{\text{in}}$:

$$\Pi = k_p \cdot f_{\Pi} \left(N_c, \beta \right) \tag{8}$$

- Isentropic efficiency η:

$$\eta = k_e \cdot f_{\eta} \left(N_c, \beta \right) \tag{9}$$

The functions $f_{\dot{m}_c}$, f_{Π} and f_{η} are constructed by bicubic Akima splines interpolating the supplied data. This results in functions that are continuously derivable with respect to N_c and β. The constant factors k_f, k_p and k_e are included in order to allow for map scaling and calibration.

A β-grid, an auxiliary coordinate system, as described by Walsh and Fletcher [28], is introduced to represent regions where the pressure ratio cannot be uniquely determined as a function of flow. This is relevant at choked flow conditions, where the speedlines are nearly vertical. Fig. 3 shows the performance map of compressor 1 with a β-grid. Eq. (10) is used to transform a compressor map onto a β-grid:

$$\Pi = (1 - \beta) \cdot \left(a_0 \dot{m}_c^{b_0} + 1 \right) + \beta \cdot \left(a_1 \dot{m}_c^{b_1} + 1 \right) \tag{10}$$

The β-grid is spanned by two polynomials of the type $a_i \dot{m}_c^{b_i} + 1$. These polynomials are positioned near the first and last available speedline data points by appropriately selecting the coefficients a_0, b_0, a_1, b_1. For each combination of N_c and β, a root finding algorithm is used to find the values for Π and $\dot{m}_c$ that satisfy Eq. (10). This is equivalent to determining the points of intersection between speedlines and β-lines depicted in Fig. 3. The resulting values are stored in $(n_\beta \times n_{N_c})$ matrices $F_{\dot{m}_c}$, F_{Π} and F_{η}, with n_β being the number of β-lines and n_{N_c} the number of speed lines. These matrices are ultimately converted to the functions in Eqs. (7), (8) and (9).

The surge margin (SM) quantifies the distance of an operating point to the surge line. This study employs a flow-based definition of SM, as given in Eq. (11) and shown in Fig. 3, due to the relatively "flat" speed lines of the radial compressors used in the heat pump system. A small constant ϵ is added to the denominator to avoid division-by-zero at zero flow (e.g. at plant start-up).

$$\text{SM} = \frac{\dot{m}_{c,\text{OP}} - \dot{m}_{c,\text{SL}}}{\dot{m}_{c,\text{OP}} + \epsilon} \tag{11}$$

The compressor model connects to a model of the motor-driven drive system with two compressor shafts and gears, accounting for rotational inertia and gear slip. A proportional–integral (PI) controller controls the shaft speed by applying torque to the drive system.

3.1.2. Turbine

Turbine performance is modeled through a map-based approach similar to the compressor model, but with two maps instead of three. The corrected mass flow rate $\dot{m}_c$ and isentropic efficiency η are modeled as functions of pressure ratio Π and corrected speed N_c:

$$\dot{m}_c = k_f \cdot f_{\dot{m}_c} \left(\Pi, N_c \right) \tag{12}$$

$$\eta = k_e \cdot f_{\eta} \left(\Pi, N_c \right) \tag{13}$$

The factors k_f and k_e allow for scaling of the turbine map. Turbine maps do not require an auxiliary β-grid, as $\dot{m}_c$ remains well-defined with respect to Π. The turbine operates in two regimes: unchoked and choked, with the latter occurring at pressure ratios higher than 2.

The turbine model is connected to a generator system model, which includes the generator and a gearbox. The generator, represented in the model by a variable external torque, recovers power from the turbine shaft by applying a negative torque to it. The gear transmits the rotational motion from the turbine to the generator, with transmission ratios that account for both the gear ratio and slip.

3.2. Piping

The system's volume dynamics, thermal inertia, pressure losses, and thermal losses are significantly influenced by the extensive network of pipes, as illustrated in Fig. 1. The pipe volumes between the heat pump components are aggregated and modeled by the Buildings library's `MixingVolume` model using dynamic balance equations for energy and mass.

$$\frac{\partial m}{\partial t} = \dot{m}_{\text{in}} + \dot{m}_{\text{out}} \tag{14}$$

$$m = V \cdot \rho(p, h) \tag{15}$$

Eq. (14) represents the mass balance, with m denoting the fluid mass within the volume. The relationship between volume V, density ρ and mass m is defined by Eq. (15) where ρ is dependent on the pressure and specific enthalpy. Together, these equations enable the volume models to simulate the heat pump's volume dynamics. Additionally, the pipe volume models are connected to a lumped heat capacity model (from the Modelica Thermal package) which also exchanges heat with the ambient assuming a constant thermal resistance between pipe surface and ambient air.

Pressure losses are calculated using the `PressureDrop` model from the Buildings library. This model assumes that the total pressure drop is the sum of a quadratic and linear correlation, as described in Eq. (16).

$$\Delta p = \Delta p_{\text{quad}} \left(\frac{\dot{m}}{\dot{m}_{\text{quad}}} \right)^2 + \Delta p_{\text{lin}} \frac{\dot{m}}{\dot{m}_{\text{lin}}} \tag{16}$$

The parameters $\dot{m}_{\text{quad}}$, $\dot{m}_{\text{lin}}$, Δp_{quad} and Δp_{lin} represent the nominal conditions, which serve as the basis for calculating pressure losses at other operating points. In the presented model, $\dot{m}_{\text{quad}} = \dot{m}_{\text{lin}}$ is assumed and assigned an arbitrary nominal value. Δp_{quad} and Δp_{lin} are calibrated using measurement data.
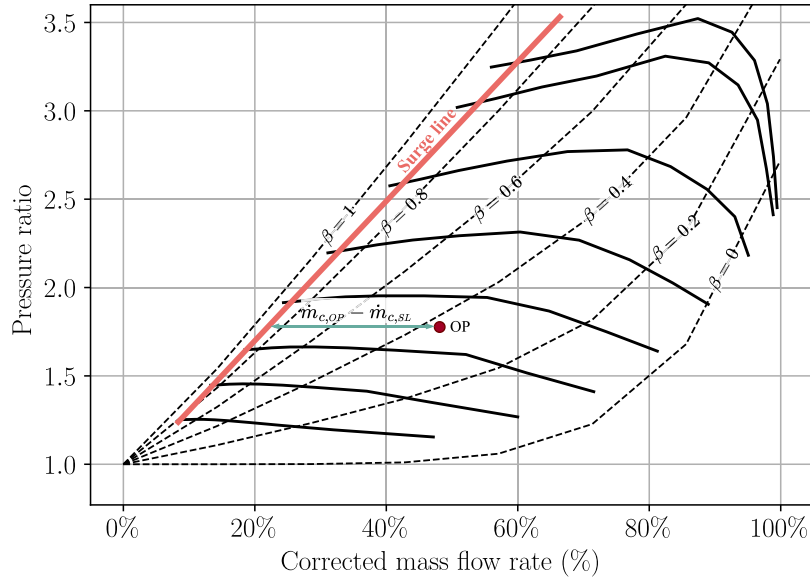
Fig. 3. Performance map of the first compressor with β-lines and exemplary surge margin.

3.3. Heat exchangers

The model for the heat exchangers is based on the `BasicHX` model from the Modelica Standard Library. Given that the thermal inertia of the heat pump is mainly determined by the heat exchangers, a detailed modeling approach was chosen. The heat exchangers are modeled using a flow scheme where the flows and the heat exchanger tube and shell material are discretized into a selectable number of 1D segments. The model is configured as a pipe-wall-pipe-wall system depicted in Fig. 4 with countercurrent flows. Each pipe and wall is discretized into six segments, a number found to reasonably balance accuracy and numerical complexity. Each segment is equipped with dynamic balance equations for mass, momentum and energy included in the DynamicPipe model from the Modelica Fluid package. These balance equations are complemented by flow models and heat transfer models which determine the pressure losses along a segment and the heat exchange with the surrounding walls. The geometry and material properties of the tubes and shell were sourced from manufacturer data sheets. Thermal conduction between wall segments is neglected.

Flow models and heat transfer models can be configured independently for each flow side of the heat exchanger. A flow model equivalent to Eq. (16), using nominal pressure loss values is selected for all heat exchanger flows.

As shown in Fig. 4, four heat transfer models are configured for the heat exchanger, determining the heat transfer coefficients, α, between the tube flow, tube walls, shell flow, shell walls, and ambient air. The heat transfer area A is defined independently of the geometry used in the flow models, enabling simplified flow models while maintaining an accurate heat transfer model. For tube flow to tube wall heat transfer, α is calculated from Eq. (17), which employs a Nusselt number correlation, f, expressed as a function of Reynolds and Prandtl numbers. For f, the Gnielinski correlation [29] for turbulent tube flow given in Eq. (18) and (19) is assumed. The resulting Nusselt number is then scaled by a calibration factor, k_h, to allow for model adjustment and calibration against experimental data. The characteristic length L and the thermal conductivity λ, which appear in Eq. (17), are derived from the heat exchanger tube geometry and material properties.

$$\mathrm{Nu} = \frac{\alpha L}{\lambda} = k_h \cdot f(\mathrm{Re}, \mathrm{Pr}) \tag{17}$$

$$f(\mathrm{Re}, \mathrm{Pr}) = \frac{(\xi/8)\,\mathrm{Re}\,\mathrm{Pr}}{1 + 12.7\sqrt{\xi/8}\left(\mathrm{Pr}^{2/3} - 1\right)}\left[1 + \left(\frac{d_i}{L}\right)^{2/3}\right] \tag{18}$$

$$\xi = \left(1.8\log_{10}\mathrm{Re} - 1.5\right)^{-2} \tag{19}$$

For the remaining heat transfers $\dot{Q}_2$, $\dot{Q}_3$ and $\dot{Q}_A$, constant values for α are assumed. The tube flow is modeled directly based on the geometry of the heat exchanger tubes. In contrast, the shell flow, owing to the complexity of tube bundle flows, is approximated by a tube flow representation. The baffled shell flow has also been neglected and simplified to a pure counterflow configuration.

3.4. Electric heaters

The electric heaters, located in the heat source and upstream of the compressor, are modeled using the `Heater_T` component from the Buildings library. This model adds a heat flow rate to maintain the set-point temperature at the heater outlet, subject to the heater's capacity limit. The inherent dynamics of the heater, arising from its thermal mass and control system, are quantified by specifying a time constant, which serves as an indicator of the system's response time.

3.5. Control valves

Valve models from the Buildings library [12] are used to model the turbine bypass valve and the three-way valve. The mass flow rates through the valves are calculated using Eq. (20) where Φ represents the valve characteristic, A_v is the valve flow coefficient, Δp is the pressure drop across the valve and ρ_{std} is the reference density.

$$\dot{m} = \Phi \cdot A_v \sqrt{\Delta p \cdot \rho_{\mathrm{std}}} \tag{20}$$

The valve flow coefficient A_v is correlated to the valve throat area, and its value derived from manufacturer data sheets. Valve characteristics were also sourced from manufacturer data, assuming an equal-percentage characteristic for the turbine bypass valve and linear characteristics for the three-way valve.

The fluid inventory valves are modeled as idealized mass flow rates injected into the low-pressure section or released from the high-pressure section of the heat pump. A PI controller regulates the valve mass flow rates to maintain the set-point pressure at the compressor inlet. A more detailed modeling approach was avoided for the fluid inventory valves, as the analysis of the fluid inventory control system is not in the scope of this study.
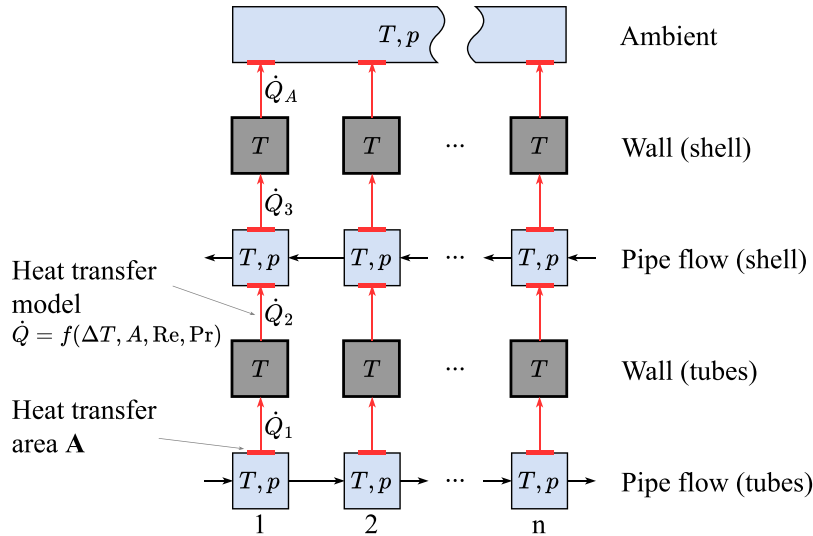
Fig. 4. Discretization scheme of the heat exchanger model.

3.6. Heat sink and source air supply system

The fans driving the secondary air flows are modeled using flow-controlled mover models from the Buildings library. These models come with default pressure curves and efficiency correlations, so the only required inputs are the nominal mass flow rate and the nominal pressure head. The fan models use mass flow rate as an input, which simplifies numerical calculations and calibration compared to models that rely on speed as an input.

The heat sink fan draws air from a boundary source with constant temperature and pressure, which can be adjusted to reflect the ambient conditions during heat pump operation. Components related to air drying and buffering have not been modeled, instead assuming reservoirs of dry air at nominal pressure.

The heat source is modeled as a closed-loop system comprising a fan, heater, and heat exchanger, reflecting the actual system configuration.

3.7. Medium model

The simulation model uses the DryAirNasa model from the Modelica Media library to represent the working medium, dry air. The model calculates thermodynamic properties based on polynomials with NASA Glenn coefficients, which assume ideal gas behavior and are valid over a temperature range of approximately 200 K to 6000 K.

3.8. Control signals and boundary conditions

The plant has numerous components that require a continuous control signal from the operator or a controller. The control input signals are organized in a signal bus (or *expandable connector*) with the minimum set of signals shown in Table 1.

Additionally, ambient and initial conditions for the simulation can be specified through boundary conditions, allowing for configuration of various simulation scenarios such as cold start, warm start, and more.

3.9. Simulation

The component models described above are integrated into the overall heat pump model. The relationship between component models is defined by the flow, thermal and signal connectors. During model translation, a process known as *model flattening* [30] is applied,

Table 1
Input signals and boundary conditions for the model.

Input signals	Symbol
Motor speed[SP]	N_M
Generator speed[SP]	N_G
Bypass valve opening	Θ_B
Three-way valve opening	Θ_{3W}
Sink mass flow rate	$\dot{m}_{101}$
Source mass flow rate	$\dot{m}_{201}$
Primary heater temperature[SP]	$T_{S,0}$
Source heater temperature[SP]	$T_{S,201}$
Compressor inlet pressure[SP]	$P_{S,0}$
Boundary conditions	
Ambient temperature	$T_{Amb.}$
Initial temperature	T_{init}
Initial pressure	p_{init}

[SP] Signal is a set-point signal.

which converts the hierarchical, object-oriented structure into a set of differential–algebraic equations (DAEs) of the form:

$$F(\dot{x}, x, y, t) = 0. \tag{21}$$

In Eq. (21), x denotes the states, $\dot{x}$ their derivatives, y the algebraic variables and t the independent time. While Modelica also supports discrete variables d within the equation system, these are omitted here for clarity. Depending on the selected numerical solver, the DAE may be transformed into an index-1 DAE

$$\dot{x} = f(x, y, t) \tag{22}$$

$$0 = g(x, y, t), \tag{23}$$

or into an ordinary differential equation (ODE) where algebraic variables y and algebraic loops (systems of equations requiring simultaneous solution) are incorporated into $\hat{f}$:

$$\dot{x} = \hat{f}(x, t) \tag{24}$$

Furthermore, the simulation requires the specification of initial conditions for the state variables so that their initial values x_0 can be computed. Cellier and Kofman [31] provide more details on transforming and solving DAEs. Solvers for both the index-1 DAE in Eqs. (22), (23) and ODE in Eq. (24) are available in most Modelica simulation environments. The model in this study can be simulated using various solvers, including DASSL [32], IDA [33] and Radau IIA [34]. All

presented results were obtained using DASSL with a tolerance of 10^{-5}. DASSL (Differential/Algebraic System Solver) is a numerical integration algorithm that uses a variable-step, variable-order backward differentiation formula (BDF) method. While originally developed for index-1 DAEs, it can also be applied to ODEs. In this work, DASSL is applied to the ODE representation with adaptive step sizing based on error estimates.

4. Calibration

Using the dynamic model presented in the previous chapter as a foundation, the following sections focus on the process of calibrating the heat pump model, where key parameters are adjusted to match the simulation results with measurement data.

4.1. Calibration of compressor performance maps

The compressors have a major influence on the heat pump performance, making their calibration a focus of this study. Pressure and temperature measurements were taken at the inlet, intermediate duct, and outlet of the compressors, along with mass flow rate and shaft speed data. These measurements allow for the calculation of all the quantities needed in the compressor map.

Data from 14.5 h of operation over three days of testing were used for calibration. Fig. 5 shows the reference compressor maps from the manufacturer [27], alongside the measured operating points used in the calibration. Due to constraints of the drive unit, shaft speeds were limited to approximately 70 % of the maximum speed. As a result, data from the compressors' high-speed operating range were unavailable for calibration. The calibration method presented in this work aims to adjust the compressor maps with the following requirements:

1. Preserve the original map's shape to retain the general compressor characteristics.
2. Accurately predict measured operating points, minimizing discrepancies between simulated and observed data.
3. Allow plausible extrapolation into high-speed regions not covered by the measurement data.

The calibration assumes that map errors are functions of β and shaft speed. The calibrated map data matrix $F_{\text{cal.}}$ is calculated by applying correction matrices C and D on the original map data matrix F as expressed in Eq. (25):

$$F_{\text{cal.}} = C \cdot F \cdot D \tag{25}$$

$$C = \begin{bmatrix} c_1 & & \\ & \ddots & \\ & & c_{n_N} \end{bmatrix} \tag{26}$$

$$D = \begin{bmatrix} d_1 & & \\ & \ddots & \\ & & d_{n_\beta} \end{bmatrix} \tag{27}$$

When the map data F is organized as an $(n_\beta \times n_N)$ matrix, the matrices C and D are diagonal matrices of dimensions $(n_N \times n_N)$ and $(n_\beta \times n_\beta)$, respectively. The multiplication of these matrices corresponds to applying scaling factors to each column (corresponding to each speed line) and each row (corresponding to each β-line) of the map data. By constraining the entries c_i and d_i of C and D to a narrow range around 1, the adjustments made to the data are small, ensuring that the original shape of the map is largely preserved. A numerical optimization is employed to determine values for c_i and d_i that minimize the deviation between the compressor map and the measured data, quantified by the residual sum of squares. The following additional transformations are applied to the correction factor vectors:

- For the c_i correction factors, the values are replaced by a weighted average of the original value and the mean value $\sum_i c_i / n_N$. This approach is based on the assumption that all speedlines are similarly over- or underperforming relative to the original map.
- For the d_i correction factors, a Gauss filter is applied on the vector. This ensures that the resulting speedlines are smooth.

The resulting calibrated compressor maps are shown in Fig. 5. Regarding the pressure ratio, compressor 1 is slightly underperforming, whereas compressor 2 is significantly underperforming. This is also illustrated in the parity plot in Fig. 6 where measured and predicted pressure ratios are compared. After applying the calibration, the pressure ratio of nearly all operating points can be predicted with a relative error of less than 5 %. The calibration of isentropic efficiency turned out to be more challenging, as shown in the parity plot in Fig. 7. Measured efficiencies of compressor 2 were significantly lower than those reported in the original performance map. This discrepancy is mostly attributed to suboptimal inflow conditions and pressure losses in the inter-compressor duct. Changes to the compressor rotor material and volutes, made specifically for the heat pump, may also contribute to deviations from the map data. The prediction of efficiency after calibration is mostly accurate within the 5 % error band, although some operating points show much larger deviations. While operating points outside the measured regime cannot be directly verified due to technical constraints, the method's reliability is supported by the accurate prediction of measured points.

4.2. Calibration of model parameters

The model was exported as a Functional Mock-up Unit (FMU) with tunable parameters to enable optimization using the Python library SciPy. Input data for the simulations, which include the control signals described in Section 3.8, was generated using test data. An optimization algorithm was used to adjust the model parameters, aiming to minimize the error between the simulated and measured signals. Model error is quantified through the residual sum of squares, evaluated at equidistant points along the measured and simulated time series.

Optimizing all parameters in a single optimization was found to be infeasible with regard to computational time and optimization convergence. Therefore, the signals and tunable parameters were divided into four groups shown in Table 2, which were selected to minimize interactions between the groups. The signals were chosen so that, once calibrated, the model accurately predicts compressor and heat exchanger performance. The allocation of parameters to these signals was based on analysis to identify which quantities most significantly affect them. For example, mass flow rates and pressures are predominantly influenced by the interactions among the compressor, turbine, and pressure losses, which motivated the parameter selection for group A.

Due to the nearly constant inflow conditions of the first compressor throughout the tests, the components are calibrated sequentially along the heat pump flow direction. For each group, the optimization algorithm determines parameter values that minimize errors between the model and measurements. It achieves this by repeatedly adjusting and re-running the simulation model. The selected grouping allowed for efficient tuning by ensuring that the effects between groups were kept minimal, making the optimization process more manageable. To further eliminate the effects of cross-influence between groups, the routine was performed twice.

The minimization problems were solved numerically using a combination of genetic and gradient-based optimization methods: To increase the chance of finding the global optimum, the process began with a genetic algorithm for a fixed number of iterations. Specifically, the `differential_evolution` method from the SciPy library [35], which implements the algorithm developed by Storn and Price [36], was applied. The best solution obtained from this genetic algorithm was
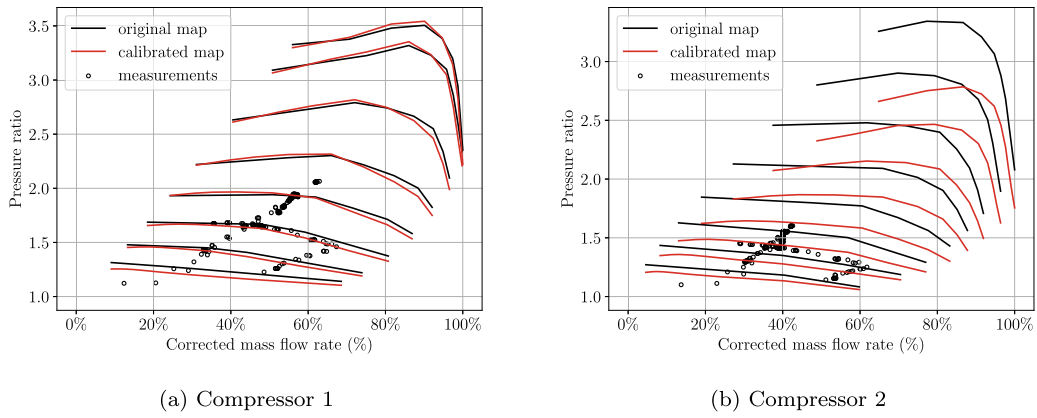
(a) Compressor 1

(b) Compressor 2

Fig. 5. Original and calibrated compressor maps with indicators for measured operating points.

(a) Compressor 1

(b) Compressor 2
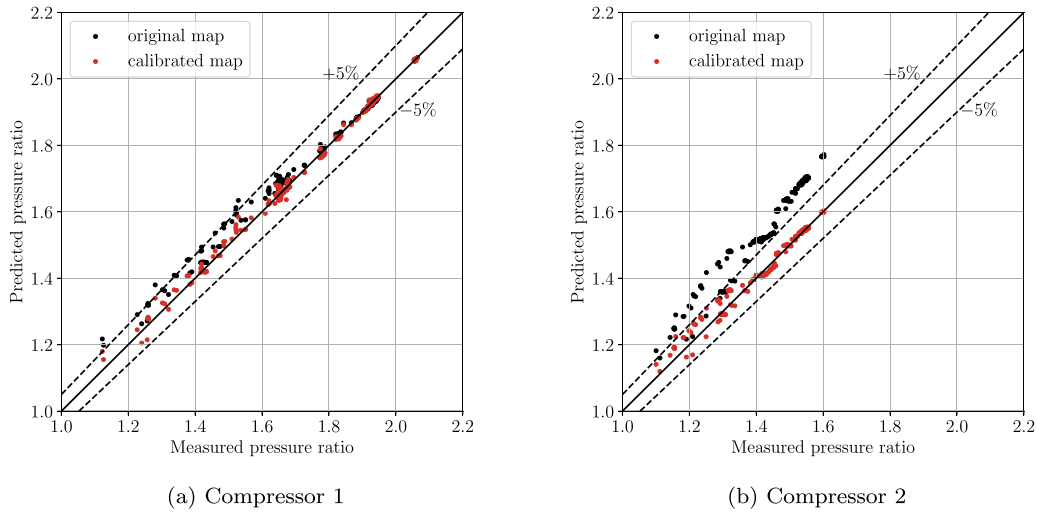
Fig. 6. Parity plot of the pressure ratio.

(a) Compressor 1

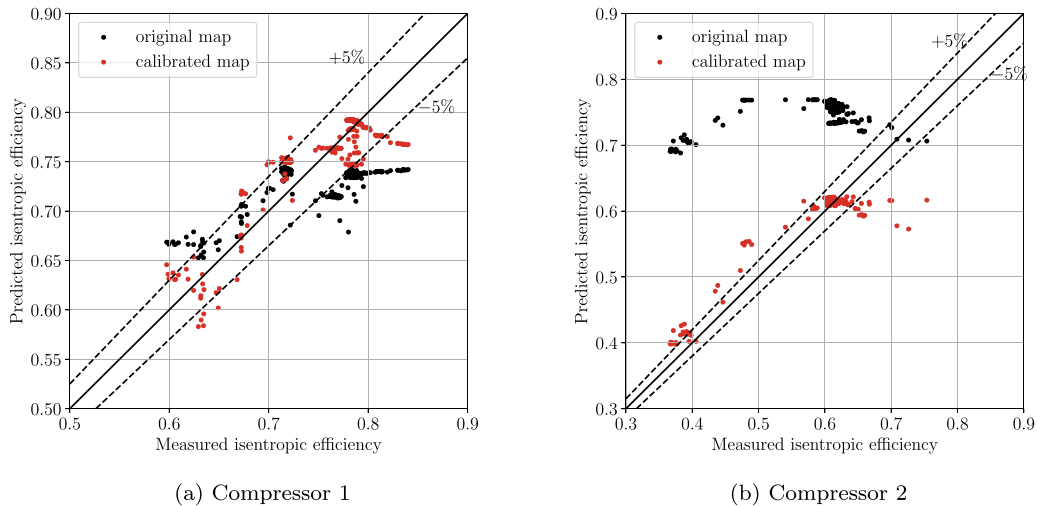(b) Compressor 2

Fig. 7. Parity plot of the isentropic efficiency.

then used as the initial guess for a gradient-based optimization, employing the Sequential Least Squares Programming (SLSQP) method [37], which produced the final solutions listed in Table 2.

The resulting nominal values for the pressure drop and map correction scalers fall within expected ranges. However, the high values

of the correction factors $k_{h,LTHX}$ and $k_{h,HTHX}$ are striking. This suggests that the heat transfer was significantly underestimated by the initially assumed Nusselt correlation prior to calibration.

After adjusting the model parameters according to Table 2, a six-hour test run with varying operating conditions was simulated to study

Table 2
Model parameter tuning.

Grp.	Signals fitted	Parameters tuned	Bounds	Final value
A	$\dot{m}$	$k_{p,C1}$	[0.97, 1.05]	1.023
	p_{0A}	$k_{p,C2}$	[0.97, 1.05]	1.042
	p_1	$k_{f,T}$	[0.97, 1.05]	1.004
		$\Delta p_{\text{lin,HP}}$	[500, 7000] Pa	6215 Pa
		$\Delta p_{\text{quad,HP}}$	[500, 7000] Pa	3050 Pa
B	T_2	$\Delta p_{\text{lin,Sink}}$	[500, 12000] Pa	3951 Pa
	T_{101}	$\Delta p_{\text{quad,Sink}}$	[500, 12000] Pa	11 747 Pa
		$k_{h,HTHX}$	[1, 30]	14.11
C	T_{4B}	$k_{e,T}$	[0.92, 1.05]	0.97
D	T_5	$\Delta p_{\text{lin,Src.}}$	[500, 6000] Pa	4583 Pa
	T_{201}	$\Delta p_{\text{quad,Src.}}$	[500, 4000] Pa	2293 Pa
		$k_{h,LTHX}$	[1, 30]	27.98

Table 3
Root mean squared error (RMSE) and mean-normalized root mean squared error (NRMSE) of the main process variables.

Measurement signal		RMSE	NRMSE
Compressor outlet	T_1	2.91 K	0.69 %
HTHX outlet	T_2	1.24 K	0.39 %
Turbine outlet	T_{4B}	1.38 K	0.53 %
LTHX outlet	T_5	0.50 K	0.17 %
HTHX inlet (sink)	T_{101}	0.57 K	0.19 %
HTHX outlet (sink)	T_{102}	1.99 K	0.50 %
LTHX inlet (source)	T_{201}	0.37 K	0.12 %
LTHX outlet (source)	T_{202}	0.76 K	0.27 %
Mass flow rate	$\dot{m}$	0.0041 kg/s	1.46 %
Compressor inlet	p_0	1203 Pa	1.18 %
Inter-compressor	p_{0A}	2388 Pa	1.37 %
Compressor outlet	p_1	3379 Pa	1.33 %

(a) Pressures

(b) Temperatures

Fig. 8. Comparison of measured and simulated values for temperatures and pressures after calibration.

the system model's dynamic responses. Fig. 8(a) shows the measured and simulated pressures upstream, in between and downstream the compressors. The results demonstrate high model accuracy, particularly at higher pressure ratios. Fig. 8(b) compares the measured and simulated temperatures at the inlets and outlets of the high-temperature heat exchanger, showing strong agreement between them. The good agreement of temperatures indicates that the model is able to capture the system's thermal inertia.

To quantify the model's predictive accuracy, root mean square error (RMSE) and mean-normalized root mean square error (NRMSE) were calculated for each process variable. RMSE, defined in Eq. (28), represents the average squared deviation between the measured data y and the simulated values $\hat{y}$, while NRMSE, defined in Eq. (29), normalizes this error relative to the mean of the measured data $\bar{y}$.
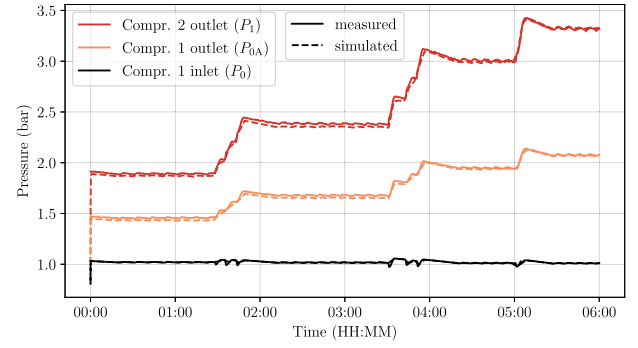
$$\text{RMSE} = \sqrt{\sum_{i=1}^{n} \frac{(y_i - \hat{y}_i)^2}{n}} \quad (28)$$

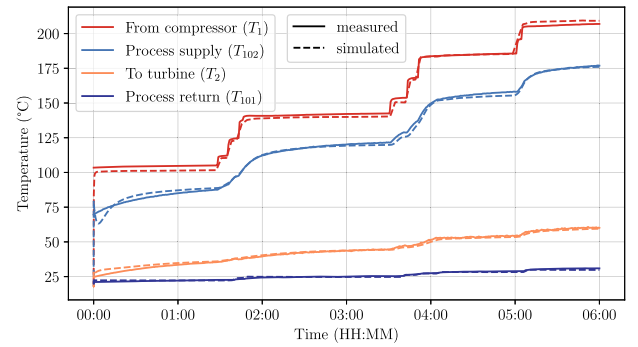$$\text{NRMSE} = \frac{\text{RMSE}}{\bar{y}} \quad (29)$$

Table 3 lists the RMSE and NRMSE values for the main process variables, assessed using 500 equidistant samples over the six-hour test period. The consistently low NRMSE values across all variables, particularly for temperatures, show that the model is capable of replicating the system's thermodynamic behavior accurately. This agreement between the model and the test data confirms the model's capability of capturing both temperature and pressure dynamics under a range of operational conditions.

5. Analysis

The validated model enables numerous possibilities to support the operation and further development of the heat pump, including control system design, condition monitoring and virtual pre-testing of plant

modifications. The following sections present the simulation of a plant cold start-up and shutdown with emphasis on investigating the effects of the system dynamics on compressor stability and heat exchanger warm-up.

5.1. Start-up and shutdown procedure

The simulated maneuver assumes ambient temperatures (15 °C) as initial conditions for all fluid and metal temperatures in the heat pump. Unlike the simulation used for model calibration, the initial fluid inventory remains unchanged throughout the entire process, with an initial pressure set at 2.7 bar, under the assumption of a perfectly sealed, air-tight heat pump system. The mass flow rates for both the heat source and heat sink are set at 0.6 kg/s.

Fig. 9 shows the motor and generator speeds during the maneuver. After initialization, the motor and generator speeds are increased from a standstill to approximately 40 %, a state referred to as Operating Point 1 (OP1). OP1 is maintained for one hour to allow the system to stabilize. Following this, the motor and generator speeds are ramped up to 80 % during a 15 min acceleration period, reaching a higher-temperature operating state, referred to as Operating Point 2 (OP2). OP2 is held constant for one hour. After this period, the motor and generator are rapidly decelerated within 30 s, returning to OP1 for the remainder of the simulation.

Fig. 10 depicts the thermodynamic cycle of the heat pump at OP1 ($t = 3700$ s) and OP2 ($t = 8100$ s). The blue cycle represents OP1, the idle operating point, which operates within a temperature and pressure range close to the initial conditions. The red cycle corresponds to OP2, the high-temperature operating point, which spans a broader range of temperatures and pressures, reaching a maximum temperature of 220 °C.
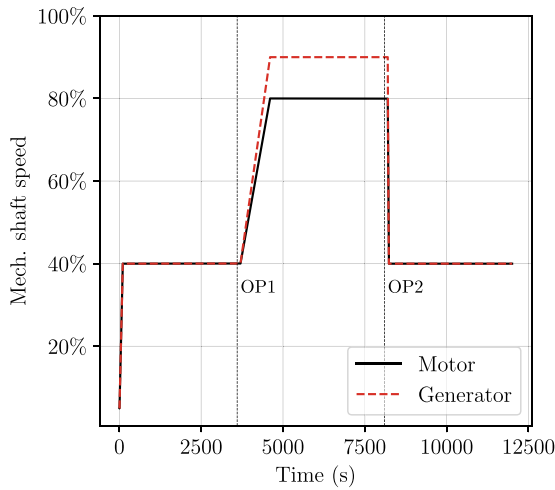
Fig. 9. Motor and generator speeds during start-up and shutdown procedure.
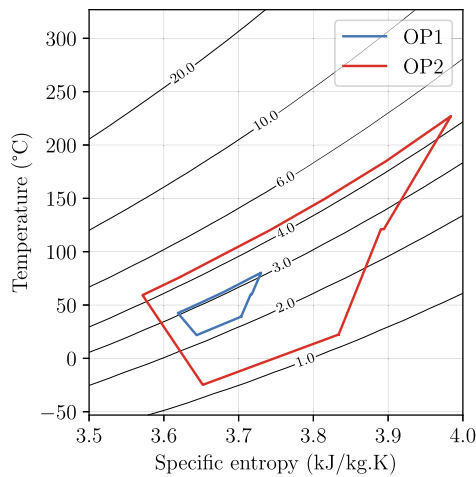

Fig. 10. Thermodynamic cycle of OP1 and OP2 in the T,s diagram.

Fig. 11 demonstrates the pressure behavior upstream, between, and downstream of the compressors throughout the simulated maneuver. With a constant fluid inventory, the heat pump's pressure levels deviate from the initial pressure as the power level increases.

5.2. Heat exchanger temperatures

Using the 1D heat exchanger model presented in Section 3.3, the dynamic temperature response of the heat exchangers can be simulated. Fig. 12 shows the air temperature of the flow into the HTHX tubes and the metal temperatures along the length of the HTHX tubes during the start-up, acceleration and deceleration phases.

The results show the effects of the large heat capacity of the heat exchanger material. Despite allowing one hour of constant control inputs at each operating point, the metal temperatures have not fully settled at steady-state conditions. This aligns with observations from heat pump testing. Notably, the temperature drop upon returning to OP1 is faster than the preceding temperature rise when transitioning to OP2. This asymmetry occurs because, during this transition, the HX tubes experience cooling from both flow sides, as the compressor outlet temperature falls to $60\,°C$, which is lower than the metal tube temperatures.

As the temperature distribution is also calculated for the HX shell, the model enables the evaluation of thermally induced mechanical tensions within the tubes. Monitoring these tensions is essential for safe operation, as they can damage the structural integrity of the heat exchanger under varying thermal loads.

5.3. Dynamic compressor stability

Fig. 13 shows the operating trajectory of the first compressor during the maneuver. When transitioning between operating points OP1 and OP2, the deceleration trajectory approaches the surge line more closely than during acceleration. This behavior results from two main factors:

- Volume dynamics: The large air volumes within the system cause pressure – and consequently, the pressure ratio – to adjust more slowly than the shaft speed.
- Thermal inertia: During deceleration, the heat exchanger retains high temperatures from the previous high-temperature operating condition. Due to choked flow conditions (constant corrected mass flow rate) in the turbine, this elevated inlet temperature reduces flow rates in accordance with Eq. (5), drawing the operating point closer to the surge line.

These mechanisms can make rapid deceleration maneuvers in heat pumps a potential concern for compressor stability. However, in the radial compressors investigated here, stability issues appear minimal, as sufficient margin from surging is maintained even under dynamic deceleration conditions. This is illustrated by Fig. 14 which shows the first compressor's surge margin during the maneuver. The rapid decrease in speed results in a temporary reduction in surge margin, before stabilizing at steady conditions.

6. Conclusion and outlook

This study presents a validated dynamic model of a high-temperature heat pump based on the Brayton cycle, implemented using Modelica. The model, calibrated with experimental data, predicts thermodynamic properties such as temperature, pressure, and flow rate variations at key locations within the heat pump. The compressor map calibration method developed in this work was used to adjust existing performance data with the available measurements and to reasonably estimate performance in regimes where measurements were not available. The calibrated map accurately matches the measured data and remains numerically robust during simulations, while preserving the original shape of the speedlines. Optimization-based tuning of compressor maps and model parameters achieved accuracy levels reflected by normalized root mean square errors (NRMSEs) ranging from $0.12\,\%$ to $1.46\,\%$. These results indicate the model's utility for studying heat pump performance across various operating conditions and support its application in designing and controlling high-temperature heat pumps for industrial use.

The model also provides insights into how the heat pump behaves during transient processes like start-up and deceleration. Simulations highlight aspects of compressor stability, including the risk of approaching surge limits during rapid decelerations. By tracking temperature changes within heat exchangers, the model can help predict thermal stresses at varying thermal loads, which is essential for maintaining system durability and safety.

In future work, the authors aim to develop a real-time version of the model that operates in parallel with the physical plant and supports continuous online calibration. This enhancement will allow the model to dynamically adjust to variations in component performance. The authors also plan to use the model to test and evaluate control systems. In particular, the model will be used as a training environment for a Reinforcement Learning (RL) agent. By leveraging RL, the aim is to develop a control system capable of handling complex dynamics more effectively than conventional methods. Such developments may contribute to improved performance and adaptability of high-temperature heat pumps in industrial contexts.
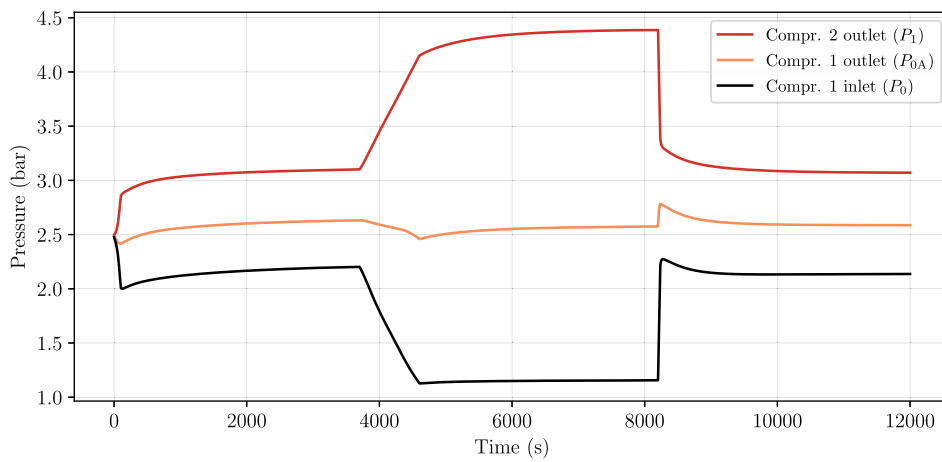
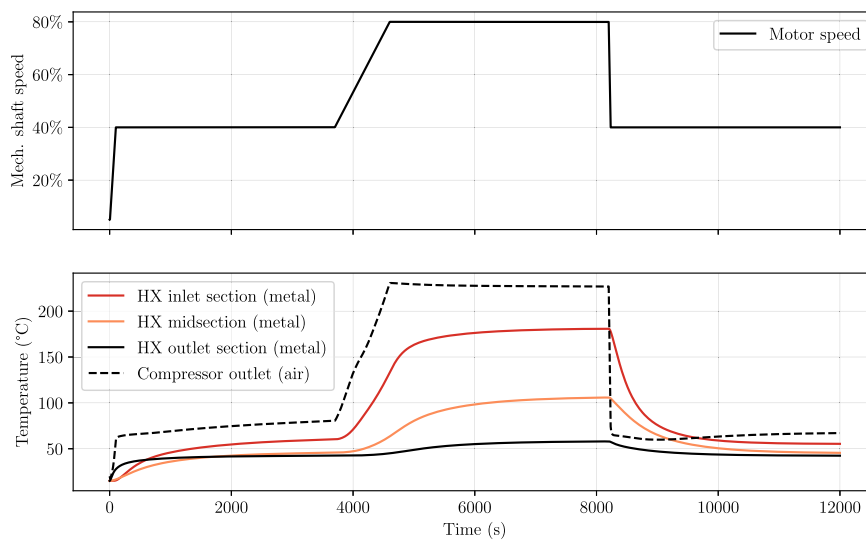**Fig. 11.** Pressures during start-up and deceleration.

Fig. 12. Simulated dynamic heat exchanger tube temperature response of the HTHX.
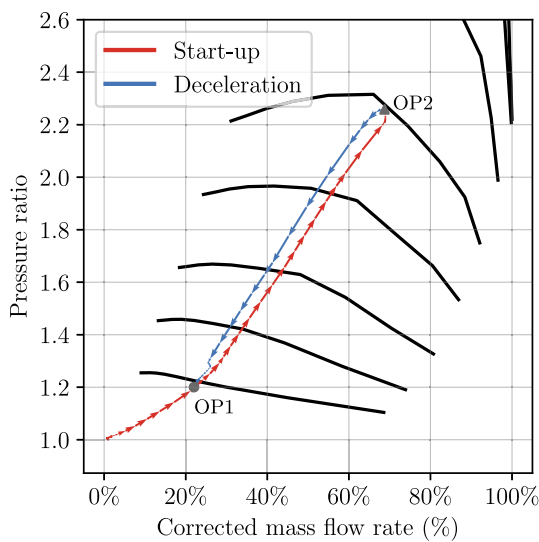

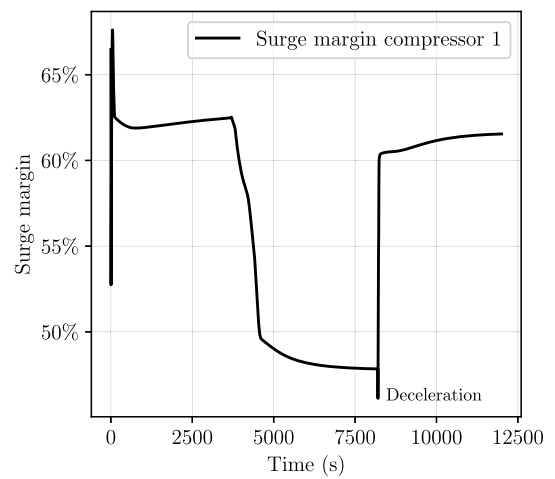**Fig. 13.** Simulated trajectory of compressor 1 during start-up and deceleration.

Fig. 14. Surge margin of compressor 1 during start-up and deceleration.

Declaration of competing interest

The authors declare that they have no known competing financial interests or personal relationships that could have appeared to influence the work reported in this paper.

Data availability

Data will be made available on request.

References

[1] IPCC, in: H. Lee, J. Romero (Eds.), Climate Change 2023: Synthesis Report: Contribution of Working Groups I, II and III to the Sixth Assessment Report of the Intergovernmental Panel on Climate Change, Intergovernmental Panel on Climate Change (IPCC), Geneva, Switzerland, 2023, http://dx.doi.org/10.59327/IPCC/AR6-9789291691647.

[2] Fraunhofer Institute for Systems and Innovation Research (ISI), Mapping and analyses of the current and future (2020 - 2030) heating/cooling fuel deployment (fossil/renewables): Prepared for: European Commission under contract N°ENER/C2/2014-641, 2016, European Commission.

[3] IEA, World Energy Outlook 2023, IEA, Paris, 2023, URL https://www.iea.org/reports/world-energy-outlook-2023.

[4] C. Arpagaus, F. Bless, M. Uhlmann, J. Schiffmann, S.S. Bertsch, High temperature heat pumps: Market overview, state of the art, research status, refrigerants, and application potentials, Energy 152 (2018) 985–1010, http://dx.doi.org/10.1016/j.energy.2018.03.166.

[5] Heat Pump Centre, IEA HPT annex 58: High-temperature heat pumps, 2023, URL https://heatpumpingtechnologies.org/annex58/.

[6] X. Ma, Y. Du, T. Zhao, T. Zhu, B. Lei, Y. Wu, A comprehensive review of compression high-temperature heat pump steam system: Status and trend, Int. J. Refrig. 164 (2024) 218–242, http://dx.doi.org/10.1016/j.ijrefrig.2024.04.024.

[7] A.J. White, Thermodynamic analysis of the reverse Joule–Brayton cycle heat pump for domestic heating, Appl. Energy 86 (11) (2009) 2443–2450, http://dx.doi.org/10.1016/j.apenergy.2009.02.012.

[8] B. Zühlsdorf, F. Bühler, M. Bantle, B. Elmegaard, Analysis of technologies and potentials for heat pump-based process heat supply above 150 ° C, Energy Convers. Manag.: X 2 (2019) 100011, http://dx.doi.org/10.1016/j.ecmx.2019.100011.

[9] F. Schlosser, M. Jesper, J. Vogelsang, T.G. Walmsley, C. Arpagaus, J. Hesselbach, Large-scale heat pumps: Applications, performance, economic feasibility and industrial integration, Renew. Sustain. Energy Rev. 133 (2020) 110219, http://dx.doi.org/10.1016/j.rser.2020.110219.

[10] Y. Du, J. Lin, J. Wu, C. Wang, T. Zhao, Y. Wu, Simulation and experimental study on dynamic characteristics of R290 split heat pump during start-up, Appl. Therm. Eng. 236 (2024) 121564, http://dx.doi.org/10.1016/j.applthermaleng.2023.121564.

[11] S. Jiang, Y. Yu, S. Li, S. Wang, Z. Ma, J. Wang, Simulation and optimum control of a two-stage compression air source heat pump system: A comparison of two kinds of variable volume approaches, Appl. Therm. Eng. 226 (2023) 120149, http://dx.doi.org/10.1016/j.applthermaleng.2023.120149.

[12] M. Wetter, W. Zuo, T.S. Nouidui, X. Pang, Modelica buildings library, J. Build. Perform. Simul. 7 (4) (2014) 253–270, http://dx.doi.org/10.1080/19401493.2013.765506.

[13] F. Casella, A. Leva, Modelling of thermo-hydraulic power generation processes using Modelica, Math. Comput. Model. Dyn. Syst. 12 (1) (2006) 19–33, http://dx.doi.org/10.1080/13873950500071082.

[14] TLK-Thermo GmbH, TIL suite: Modeling and simulation of thermal systems, 2023, URL https://www.tlk-thermo.com/en/software/til-suite.

[15] Modelon, Inc., Modelon library suite, 2024, URL https://modelon.com/modelon-library-suite-modelica-libraries/.

[16] J.L. Poulsen, A. Schulte, S. Försterling, W. Meesenburg, J. Koehler, J.J. Aguilera, B. Elmegaard, B. Zühlsdorf, Model-based analysis of a heat pump cascade system using seawater and ammonia as working fluids, in: 35th International Conference on Efficiency, Cost, Optimization, Simulation and Environmental Impact of Energy Systems, 2022, URL https://orbit.dtu.dk/en/publications/model-based-analysis-of-a-heat-pump-cascade-system-using-seawater.

[17] W. Meesenburg, W.B. Markussen, T. Ommen, B. Elmegaard, Optimizing control of two-stage ammonia heat pump for fast regulation of power uptake, Appl. Energy 271 (2020) 115126, http://dx.doi.org/10.1016/j.apenergy.2020.115126.

[18] L. Wolscht, K. Knobloch, E. Jacquemoud, P. Jenny, Dynamic simulation and experimental validation of a 35 MW heat pump based on a transcritical CO2 cycle, Energy 294 (2024) 130897, http://dx.doi.org/10.1016/j.energy.2024.130897.

[19] J.J. Aguilera, R. Padullés, W. Meesenburg, W.B. Markussen, B. Zühlsdorf, B. Elmegaard, Operation optimization in large-scale heat pump systems: A scheduling framework integrating digital twin modelling, demand forecasting, and MILP, Appl. Energy 376 (2024) 124259, http://dx.doi.org/10.1016/j.apenergy.2024.124259.

[20] H. Yang, J. Li, Z. Ge, L. Yang, X. Du, Dynamic characteristics and control strategy of pumped thermal electricity storage with reversible Brayton cycle, Renew. Energy 198 (2022) 1341–1353, http://dx.doi.org/10.1016/j.renene.2022.08.129.

[21] H. Yang, J. Li, Z. Ge, L. Yang, X. Du, Dynamic performance for discharging process of pumped thermal electricity storage with reversible Brayton cycle, Energy 263 (2023) 125930, http://dx.doi.org/10.1016/j.energy.2022.125930.

[22] G.F. Frate, M. Pettinari, E. Di Pino Incognito, R. Costanzi, L. Ferrari, Dynamic Modelling of a Brayton PTES System, in: Volume 4: Cycle Innovations; Cycle Innovations: Energy Storage, American Society of Mechanical Engineers, 2022, http://dx.doi.org/10.1115/GT2022-83445.

[23] T. Zhao, H. Li, X. Li, Q.-H. Sun, X.-Y. Fang, H. Ma, Q. Chen, A frequency domain dynamic simulation method for heat exchangers and thermal systems, Energy 286 (2024) 129552, http://dx.doi.org/10.1016/j.energy.2023.129552.

[24] Y. Wang, X. Wang, Z. Wang, B. Zhao, J. Xu, Y. Zhao, A novel method for aero-engine map calibration using adaptation factor surface, Meas. 239 (2025) 115394, http://dx.doi.org/10.1016/j.measurement.2024.115394.

[25] J. Oehler, A.P. Tran, P. Stathopoulos, Simulation of a safe start-up maneuver for a brayton heat pump, in: Volume 4: Cycle Innovations; Cycle Innovations: Energy Storage, American Society of Mechanical Engineers, 2022, http://dx.doi.org/10.1115/GT2022-79399.

[26] M. Pettinari, G.F. Frate, L. Ferrari, F.C. Yücel, A.P. Tran, P. Stathopoulos, K.G. Kyprianidis, Thermal load control in high-temperature heat pumps: a comparative study, J. Eng. Gas Turbines Power (2024) 1–40, http://dx.doi.org/10.1115/1.4066706.

[27] ASA Kompressor GmbH, The ASA supercharger T1, URL https://asa-kompressor.com/en/products/supercharger-t1/.

[28] P.P. Walsh, P. Fletcher, Gas Turbine Performance, second ed., Blackwell Science, Malden, MA, 2008, http://dx.doi.org/10.1002/9780470774533.

[29] VDI heat atlas, second ed., in: Springer reference, Springer, Verein Deutscher Ingenieure, Heidelberg, 2010.

[30] Modelica Association, in: H. Olsson (Ed.), Modelica® – A Unified Object-Oriented Language for Systems Modeling: Language Specification Version 3.6, 2023, URL https://specification.modelica.org/maint/3.6/MLS.pdf.

[31] F.E. Cellier, E. Kofman, Continuous System Simulation, first ed., Springer, New York, NY, 2005.

[32] L.R. Petzold, Description of DASSL: a Differential/algebraic System Solver, Sandia National Labs., Livermore, CA (USA), 1982.

[33] A.C. Hindmarsh, P.N. Brown, K.E. Grant, S.L. Lee, R. Serban, D.E. Shumaker, C.S. Woodward, SUNDIALS: Suite of nonlinear and differential/algebraic equation solvers, ACM Trans. Math. Softw. 31 (3) (2005) 363–396, http://dx.doi.org/10.1145/1089014.1089020.

[34] E. Hairer, G. Wanner, Stiff differential equations solved by Radau methods, J. Comput. Appl. Math. 111 (1–2) (1999) 93–111, http://dx.doi.org/10.1016/S0377-0427(99)00134-X.

[35] P. Virtanen, R. Gommers, T.E. Oliphant, M. Haberland, T. Reddy, D. Cournapeau, E. Burovski, P. Peterson, W. Weckesser, J. Bright, S.J. van der Walt, M. Brett, J. Wilson, K.J. Millman, N. Mayorov, A.R.J. Nelson, E. Jones, R. Kern, E. Larson, C.J. Carey, İ. Polat, Y. Feng, E.W. Moore, J. VanderPlas, D. Laxalde, J. Perktold, R. Cimrman, I. Henriksen, E.A. Quintero, C.R. Harris, A.M. Archibald, A.H. Ribeiro, F. Pedregosa, P. van Mulbregt, SciPy 1.0: fundamental algorithms for scientific computing in Python, Nat. Methods 17 (3) (2020) 261–272, http://dx.doi.org/10.1038/s41592-019-0686-2.

[36] R. Storn, K. Price, Differential evolution – A simple and efficient heuristic for global optimization over continuous spaces, J. Glob. Optim. 11 (4) (1997) 341–359, http://dx.doi.org/10.1023/A:1008202821328.

[37] D. Kraft, A software package for sequential quadratic programming, in: Deutsche Forschungs- und Versuchsanstalt für Luft- und Raumfahrt Köln: Forschungsbericht, Wiss. Berichtswesen d. DFVLR, 1988.